

LERD: Latent Event-Relational Dynamics for Neurodegenerative Classification

Hairong Chen^{*1,2} Yicheng Feng^{*3} Ziyu Jia^{2,4} Samir Bhatt^{3,5} Hengguan Huang^{3,5}

Abstract

Alzheimer’s disease (AD) alters brain electrophysiology and disrupts multichannel EEG dynamics, making accurate and clinically useful EEG-based diagnosis increasingly important for screening and disease monitoring. However, many existing approaches rely on black-box classifiers and do not explicitly model the underlying dynamics that generate observed signals. To address these limitations, we propose LERD, an end-to-end Bayesian electrophysiological neural dynamical system that infers latent neural events and their relational structure directly from multichannel EEG without event or interaction annotations. LERD combines a continuous-time event inference module with a stochastic event-generation process to capture flexible temporal patterns, while incorporating an electrophysiology-inspired dynamical prior to guide learning in a principled way. We further provide theoretical analysis that yields a tractable bound for training and stability guarantees for the inferred relational dynamics. Extensive experiments on synthetic benchmarks and two real-world AD EEG cohorts demonstrate that LERD consistently outperforms strong baselines and yields physiology-aligned latent summaries that help characterize group-level dynamical differences.

1. Introduction

Alzheimer’s disease (AD) is a progressive neurodegenerative disorder and a major cause of dementia worldwide, with enormous personal and societal costs. Electroencephalography (EEG) offers a non-invasive, low-cost and widely available window into AD-related brain dysfunction. Decades of work have established robust macroscopic signatures, most notably *oscillatory slowing*, increased delta/theta power and reduced alpha/beta power, alongside alterations in large-scale interactions and synchrony across cortical regions (Jeong, 2004; Dauwels et al., 2010; Babiloni et al., 2021). These findings have motivated a growing interest in using EEG not only for automated AD assessment but also for mechanistic insight into how neural activity and network dynamics are disrupted over the course of the disease.

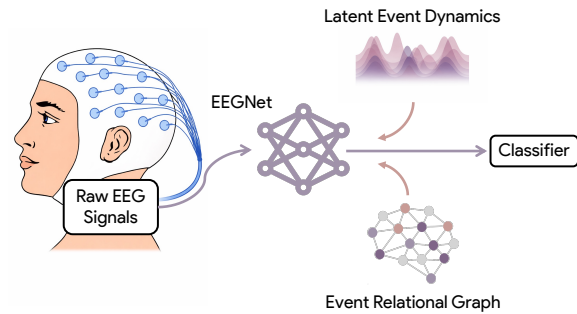


Figure 1. Overview of the LERD pipeline

Deep learning has substantially advanced EEG-based AD classification and staging. Convolutional and recurrent architectures, as well as graph- and transformer-based models, can ingest multichannel time series or time–frequency representations and achieve strong diagnostic performance (Ieracitano et al., 2020; Pineda et al., 2019; Vicchiotti et al., 2023; Tawhid et al., 2025). Yet, most existing pipelines are designed as *black-box classifiers* optimized primarily for accuracy from hand-crafted or learned features. They map rich spatiotemporal signals to labels, but typically do not model how *latent neural events* and *interaction patterns* unfold and interact in time (Ehteshamzad et al., 2024; Acharya et al., 2025; Wang et al., 2024; Klepl et al., 2024). As a result, it remains difficult to relate model predictions back

^{*}Equal contribution ¹Institute of Information Science, Beijing Jiaotong University, Beijing, China ²Brainnetome Center, Institute of Automation, Chinese Academy of Sciences, Beijing, China ³Section of Health Data Science & AI, Department of Public Health, University of Copenhagen, Copenhagen, Denmark ⁴Beijing Key Laboratory of Brainnetome and Brain-Computer Interface ⁵MRC Centre for Global Infectious Disease Analysis, Department of Infectious Disease Epidemiology, School of Public Health, Faculty of Medicine, Imperial College London, London, United Kingdom. Correspondence to: Ziyu Jia <jia.ziyu@outlook.com>, Samir Bhatt <samir.bhatt@sund.ku.dk>, Hengguan Huang <hengguan.huang@sund.ku.dk>.

Preprint. February 23, 2026.

to dynamical structures that neuroscientists and clinicians can compare against established EEG phenomena, such as event-driven activity patterns, effective connectivity and their disease-related distortions.

Building such a unifying, electrophysiology-aware dynamical framework is challenging for at least two reasons. First, scalp EEG is a noisy, frequency-dependent *linear mixture* of mesoscopic sources; reconstructing latent population activity from sensor-level data is an ill-posed inverse problem highly sensitive to modeling assumptions and head conductivity estimates (Michel & Brunet, 2019; Michel et al., 2004). Second, widely used interaction metrics suffer from *interpretational pitfalls*; volume conduction, common input and signal-to-noise differences can all induce spurious or inconsistent connectivity estimates across analysis pipelines unless dynamics and biophysical constraints are handled explicitly (Bastos & Schoffelen, 2016; Mahjoory et al., 2017). Together, these issues make it nontrivial to infer meaningful latent dynamics and directed graphs directly from raw or minimally processed EEG.

These observations raise a set of fundamental questions for EEG-based modeling of AD. *First*, can we design a neural dynamical system that infers latent, event-based activity trajectories directly from multichannel EEG, while respecting basic electrophysiological constraints such as plausible firing rates, refractory behavior and frequency ranges? *Second*, can we recover a directed, event-level interaction graph that captures how events in one channel probabilistically influence future events in others, in a way that is robust to mixing and noise and does not require spike or edge annotations? *Third*, can such a model simultaneously yield latent dynamical structure that supports scientific analysis and competitive performance on practical tasks, such as characterizing AD-related changes in network dynamics and improving EEG-based AD assessment?

We address these questions with **LERD**, a *Bayesian electrophysiological neural dynamical system* that infers event-driven latent dynamics and a conditional interaction graph directly from EEG, as shown in Figure 1. At its core, LERD represents per-channel activity with an **Event Posterior Differential Equation (EPDE)**, whose solution provides a continuous-time representation of latent dynamics and expected next-event times. These expectations parameterize a **Mean-Evolving Lognormal Process (MELP)** that samples inter-event intervals from a log-normal mixture via reparameterized sampling, enabling flexible yet tractable modeling of event statistics. To encode electrophysiological knowledge, we introduce a differentiable **leaky-integrate-and-fire (dLIF) prior** that imposes leak, refractory and rate constraints as well as plausible frequency ranges on the latent process. Finally, LERD infers a directed **event-relational graph (ERG)** by mapping cross-channel

event lags through a smooth nonlinearity into edge weights, thereby capturing how events in one channel influence the timing of events in others. The entire model is trained end-to-end under a variational inference framework, for which we derive a tractable initial value problem (IVP)-based upper bound for the event-prior KL under the dLIF rate, and we establish stability guarantees for the inferred ERG with respect to lag noise.

Importantly, our use of electrophysiology-inspired dLIF prior is *phenomenological* rather than a claim that scalp EEG directly reflects single-neuron dynamics. Scalp EEG has high temporal resolution (millisecond scale) but limited spatial specificity; we therefore treat the dLIF component as a structured prior on *population-level* latent rate dynamics (e.g., leak/refractory constraints), used to regularize an otherwise flexible neural dynamical system.

Major Contributions.

- We propose **LERD**, a unified Bayesian neural dynamical system that infers latent event processes and event-relational graph dynamics directly from multichannel EEG, without requiring spike or edge annotations.
- We incorporate an electrophysiology-informed **dLIF prior** into training, providing biophysically meaningful constraints on rates, refractoriness and frequency content of the inferred latent dynamics.
- We develop theory establishing a computationally tractable IVP-based upper bound for the variational learning objective and a stability bound for LERD’s inferred event-relational graph dynamics.
- We provide empirical evidence that LERD (i) accurately recovers latent event and graph dynamics that shed light on AD-related alterations in neural activity and interactions, and (ii) achieves superior performance over strong baselines on both synthetic benchmarks and real AD EEG datasets.

2. Related Work

2.1. EEG-based AD diagnosis with supervised pipelines

A large body of work frames EEG-based analysis of Alzheimer’s disease (AD) as a supervised classification problem, where hand-crafted spectral or connectivity features (e.g., band power, topographies, and simple graph summaries) are extracted from multichannel recordings and then fed into conventional classifiers (Ieracitano et al., 2020). Recent studies further benchmark alternative feature-classifier combinations and examine protocol choices such as task versus resting-state recordings (Vicchiotti et al., 2023; Kim

et al., 2024). While these pipelines can achieve strong diagnostic accuracy, they typically summarize EEG into static descriptors and do not explicitly model the latent, event-driven dynamics and directed interactions that generate the signals. More recent studies continue to refine supervised AD–EEG pipelines with stronger models and evaluation protocols (Vicchiotti et al., 2023; Kim et al., 2024; Tawhid et al., 2025).

2.2. EEG dynamics and latent structure modeling

A complementary line of work seeks to model EEG dynamics more directly from a dynamical-systems perspective, emphasizing rapidly switching, whole-brain patterns and their temporal organization. EEG microstate analysis characterizes ongoing activity as sequences of quasi-stable scalp topographies (typically $\sim 60\text{--}120$ ms) and provides an interpretable window into transient large-scale network dynamics (Michel & Koenig, 2018). Complementarily, Hidden Markov Modelling has been used to infer fast transient EEG network states and their transition structure (Hunyadi et al., 2019).

Despite this progress, many dynamical approaches still operate on continuous-valued latent trajectories and do not explicitly recover directed, event-level interactions that explain how activity in one region influences future dynamics in others. Generative biophysical models such as dynamic causal modeling (DCM) provide a principled route to infer effective connectivity from EEG/MEG, but they typically require specifying an explicit neural mass model and a priori network structure (Kiebel et al., 2009). As a result, bridging transient EEG state dynamics with directed, event-driven interaction structure remains an open challenge.

3. Problem Formulation

We study *unsupervised* latent–event and relation discovery in multichannel time series with *sequence-level* labels. Given a dataset $\mathcal{D} = \{(X^{(n)}, Y^{(n)})\}_{n=1}^N$ where $X^{(n)} = \{x_c^{(n)}\}_{c=1}^C$ (e.g., multichannel EEG) and $Y^{(n)} \in \mathcal{Y}$ (e.g., AD vs. control), and *no* supervision on per-channel events or inter-channel relations, our goal is to infer (i) channel-wise latent event times $T_c^{(n)} = \{t_{c,k}^{(n)}\}$ summarized by posterior event-time distributions $\mathbf{p}^{(n)}(t) = \{p_c^{(n)}(t)\}_{c=1}^C$, and (ii) a (possibly time-varying) relational structure represented as a graph process $G^{(n)}(t)$ with adjacency $A^{(n)}(t) \in \mathbb{R}^{C \times C}$. We aim to recover $\{\mathbf{p}^{(n)}(t)\}_{n=1}^N$ and the conditional graph dynamics $P(G^{(n)}(\cdot) | \mathbf{p}^{(n)}(\cdot))$ from $\{X^{(n)}\}_{n=1}^N$, and use the inferred events/graphs as inputs to a predictor of $Y^{(n)}$; importantly, $Y^{(n)}$ provides only sequence-level supervision and does not directly label events or edges.

4. Bayesian Neural Dynamical System

4.1. Overview

We introduce LERD, a Bayesian neural dynamical system for multichannel sequences that represents each channel with a latent *event* process and couples channels through a conditional *event–relational graph* (ERG) driven by the timing and ordering of inferred events. This design targets settings where clinically relevant information lies in *when* events occur and *how* they align across channels. In particular, our graph estimation follows the spike-timing-dependent plasticity (STDP) principle that coupling depends on relative spike timing, with near-coincident pre/post spikes inducing stronger interaction (Bi & Poo, 1998; Feldman, 2012); accordingly, we construct edges as a smooth function of cross-channel event-time lags implied by the inferred event posteriors.

At a high level, LERD has three interacting components. First, an *event posterior differential equation* (EPDE) encodes per-channel event dynamics by producing posterior event-time distributions (equivalently, an approximate posterior over latent event times $\{T_c^{(n)}\}$) conditioned on the observed sequence $X^{(n)}$. Second, a *mean–evolving lognormal mechanism* (MELP) uses EPDE outputs as mean parameters to generate stochastic inter-event timing between successive latent event times $t_{c,k}^{(n)}$, ensuring positive and flexible timing statistics. Third, an *event–relational graph* $G^{(n)}(t)$ is inferred from event co-occurrence and cross-channel lags derived from the EPDE/MELP event posterior, via an STDP-shaped lag-to-edge mapping that specifies how relative event timing modulates effective coupling.

For each labeled sequence $(X^{(n)}, Y^{(n)})$, the inferred triple $(X^{(n)}, T^{(n)}, G^{(n)})$ is passed to a decoder $p_\theta(Y^{(n)} | X^{(n)}, T^{(n)}, G^{(n)})$ for downstream prediction (e.g., AD vs. control). Training is end-to-end via variational learning that jointly optimizes EPDE and MELP while learning ERG dynamics under weak regularization; details are provided in the learning subsection.

4.2. Learning

We train LERD end-to-end via variational inference by *minimizing* a negative-ELBO-style objective. For labeled data $\{(X^{(n)}, Y^{(n)})\}_{n=1}^N$, let $T^{(n)} = \{T_c^{(n)}\}_{c=1}^C$ collect all latent event times and let $\tau^{(n)} = \{\tau_{c,k}^{(n)}\}$ collect the corresponding inter-event intervals. EPDE produces posterior event-time distributions and thereby induces an approximate posterior $q_\phi(T^{(n)} | X^{(n)})$. MELP parameterizes a variational distribution over inter-event intervals $q_\phi(\tau^{(n)} | X^{(n)})$ (using EPDE outputs as its mean parameters), which we use to draw reparameterized samples that yield event-time realizations. Given sampled events, we construct an ERG $G_\eta^{(n)}$

via the lag-to-edge map $\varphi_\eta(\cdot)$, and predict labels with the decoder $p_\theta(Y^{(n)} | X^{(n)}, T^{(n)}, G_\eta^{(n)})$.

Concretely, we minimize

$$\begin{aligned} \mathcal{J}(\theta, \phi, \eta) = & \sum_{n=1}^N \left(-\mathbb{E}_{q_\phi} \left[\log p_\theta(Y^{(n)} | X^{(n)}, T^{(n)}, G_\eta^{(n)}) \right] \right. \\ & \left. + \text{KL}_{T^{(n)}}^{(n)} + \text{KL}_{\tau^{(n)}}^{(n)} + \beta \mathcal{R}_{\text{ERG}}^{(n)} + \lambda_{\text{LIF}} \mathcal{R}_{\text{LIF}}^{(n)} \right), \end{aligned} \quad (1)$$

where $\text{KL}_{T^{(n)}}^{(n)} := \text{KL}(q_\phi(T^{(n)} | X^{(n)}) \| p_{\text{dLIF}}(T))$ compares the EPDE-induced event posterior to the electrophysiology-informed prior $p_{\text{dLIF}}(T)$, and $\text{KL}_{\tau^{(n)}}^{(n)} := \text{KL}(q_\phi(\tau^{(n)} | X^{(n)}) \| p_0(\tau))$ regularizes MELP against a lognormal(-mixture) prior over inter-event intervals. The term $\mathcal{R}_{\text{LIF}}^{(n)}$ softly enforces leaky-integrate-and-fire consistency on differentiable rate proxies read out from the EPDE state, with weight $\lambda_{\text{LIF}} \geq 0$, while $\mathcal{R}_{\text{ERG}}^{(n)}$ weakly nudges ERG edges toward observable statistics computed from $X^{(n)}$ (e.g., correlation-based summaries), with strength $\beta \geq 0$.

Challenges. Three technical issues arise in optimizing (1). First, $\text{KL}_{T^{(n)}}^{(n)}$ involves *path measures* induced by a differential equation and is intractable in closed form (it integrates over an infinite-dimensional trajectory); we therefore replace it with a tractable integral-rate surrogate that depends only on the dLIF rate $r(t)$, with a formal bound given in the Theory (Appendix). Second, enforcing a LIF prior directly is difficult because the spike function in LIF is *non-differentiable*, which prevents straightforward use in gradient-based training; instead we introduce differentiable rate proxies and constrain them to follow dLIF laws via $\mathcal{R}_{\text{LIF}}^{(n)}$. Third, ERG learning lacks ground-truth edges; to avoid over-constraining the graph, we only use the weak regularizer $\mathcal{R}_{\text{ERG}}^{(n)}$ to bias edge strengths toward experimental observables, leaving the fine-grained graph structure to be driven by event lags inferred from the EPDE-MELP posterior.

4.3. Prior: Electrophysiology-informed dLIF prior

Each EEG channel can be viewed as an aggregated response of a population of neurons, where clinically relevant information is often reflected in the timing of latent neuronal events. To inject an electrophysiology-inspired inductive bias of neurons, we place a biophysical prior on event timing by instantiating each channel’s latent events $T_c^{(n)} = \{t_{c,k}^{(n)}\}$ as a renewal process whose hazard is derived from a differentiable leaky-integrate-and-fire (dLIF) abstraction (Burkitt, 2006). This prior regularizes event generation toward physiologically plausible behavior while remaining differentiable for end-to-end learning.

For channel c , the (rescaled) membrane potential evolves as

$$\frac{d}{dt} u_c(t) = b_c(t) - u_c(t), \quad b_c(t) > 1, \quad (2)$$

where $b_c(t)$ is an effective (learned) input drive. Given this membrane dynamics, the implied instantaneous *firing rate* is

$$r_c(t) = \left[-\log(1 - 1/b_c(t)) \right]^{-1}. \quad (3)$$

This rate induces a dLIF inter-event time density

$$p_{\text{dLIF},c}(t) = r_c(t) \exp\left(-\int_0^t r_c(s) ds\right), \quad (4)$$

and the resulting dLIF prior for channel c is the renewal law $p_{\text{dLIF}}(T_c^{(n)})$ with hazard $r_c(t)$. We parameterize $b_c(t)$ by a bounded neural mapping from learned embeddings, for example

$$b_c(t) = 1 + \text{softplus}(g(z_c^{(n)}(t))), \quad (5)$$

where $g(\cdot)$ is a neural network; $z_c^{(n)}(t)$ denotes features derived from $X^{(n)}$. This construction guarantees $b_c(t) > 1$ and thus $r_c(t) > 0$. Refractory effects are incorporated through a smooth gating factor $\alpha_c^{(n)}(t) \in (0, 1]$ constructed from recent events in $T_c^{(n)}$, using an effective rate $\tilde{r}_c(t) = \alpha_c^{(n)}(t) r_c(t)$ to suppress implausible near-back-to-back spikes.

Because the hard spike nonlinearity is non-differentiable, we regularize *rates* rather than spikes. Concretely, the learning objective includes a dLIF consistency term

$$\mathcal{R}_{\text{LIF}} = \sum_c \int_0^S (\hat{r}_c^{(n)}(t) - \tilde{r}_c(t))^2 dt, \quad (6)$$

where $\hat{r}_c^{(n)}(t)$ is a differentiable rate proxy read from the EPDE state for sequence n over a time horizon $[0, S]$. This encourages the learned rates to follow dLIF membrane dynamics without invoking non-differentiable spike functions (Nefcici et al., 2019). The variational KL between the EPDE-induced path law $q_\phi(T_c^{(n)} | X^{(n)})$ and $p_{\text{dLIF}}(T_c^{(n)})$ is intractable in general; we therefore use the following tractable integral-rate bound, which yields a stable surrogate for training while preserving the biophysical semantics of the prior.

Theorem 4.1 (IVP-based upper bound for the event-prior KL under dLIF rates). *Let $q(t)$ be a strictly positive, integrable density on $[0, S]$ ($0 < S \leq \infty$). Let the electrophysiology-informed prior be*

$$p_r(t) = r(t) \exp\left(-\int_0^t r(u) du\right), \quad (7)$$

where $r : [0, S] \rightarrow [a, b] \subset (0, \infty)$ is measurable with $0 < a \leq b < \infty$. Define the change of variables $m = -e^{-t} \in [-e^{-S}, -1]$ and $M = -\log(-m) = t$. Set

$$g(m) := -\frac{q(M)}{mM} \log \frac{q(M)}{Mr(M) e^{-\int_0^M r(u) du}}, \quad (8)$$

$$G'(m) = g(m), \quad G(-e^{-S}) = 0. \quad (9)$$

Then

$$\text{KL}(q \| p_r) = \int_0^S q(t) \log \frac{q(t)}{r(t)e^{-\int_0^t r}} dt = \lim_{\varepsilon \downarrow 0} G(-\varepsilon), \quad (10)$$

and for any $\varepsilon \in (0, e^{-S})$,

$$\text{KL}(q \| p_r) \leq G(-\varepsilon) + |G(-2\varepsilon) - G(-\varepsilon)| =: \mathcal{U}_\varepsilon, \quad (11)$$

with $\mathcal{U}_\varepsilon \rightarrow \text{KL}(q \| p_r)$ as $\varepsilon \rightarrow 0$.

The proofs are provided in the Appendix. In training we evaluate the KL term using the computable bound \mathcal{U}_ε from Eq. (11) (fixed small ε and an ODE solver for Eq. (9)).

4.4. Posterior: Event Posterior Differential Equation (EPDE)

For each sequence $(X^{(n)}, Y^{(n)})$ and channel c , let $q_c^{(n)}(t | x_c^{(n)})$ denote the density of the next event time given the observed channel signal $x_c^{(n)}$. If $\tilde{t}_{c,k-1}^{(n)}$ denotes the previous (predicted) event time on that channel, the expected next event time is

$$\tilde{t}_{c,k}^{(n)} = \int_{\tilde{t}_{c,k-1}^{(n)}}^{\infty} t q_c^{(n)}(t | x_c^{(n)}) dt. \quad (12)$$

To express this update via an initial value problem (IVP), we introduce an auxiliary function $\Phi_c^{(n)}(t)$ whose derivative accumulates the contribution of $q_c^{(n)}$:

$$(\Phi_c^{(n)})'(t) = -t q_c^{(n)}(t | x_c^{(n)}). \quad (13)$$

Its initial value encodes the full expectation under $q_c^{(n)}$:

$$\Phi_c^{(n)}(0) = \int_0^{\infty} t q_c^{(n)}(t | x_c^{(n)}) dt. \quad (14)$$

With this definition, the expected next event time in (12) can be written as the IVP solution evaluated at the previous event time:

$$\tilde{t}_{c,k}^{(n)} = \Phi_c^{(n)}(\tilde{t}_{c,k-1}^{(n)}). \quad (15)$$

Directly solving (13)–(15) and computing $\Phi_c^{(n)}(0)$ is intractable, so we approximate this mapping with a differentiable neural surrogate that updates the predicted next event time:

$$\tilde{t}_{c,k}^{(n)} = f_{\theta_\Phi}(\tilde{t}_{c,k-1}^{(n)}, x_c^{(n)}), \quad (16)$$

implemented to ensure $\tilde{t}_{c,k}^{(n)} > \tilde{t}_{c,k-1}^{(n)}$, so that latent events remain strictly ordered in time.

Consequently, differentiating the ideal $\Phi_c^{(n)}(t)$ with respect to t yields an *event-time posterior* of the form

$$q_c^{(n)}(t | x_c^{(n)}) = -\frac{(\Phi_c^{(n)})'(t)}{t}, \quad (17)$$

which we approximate with the EPDE parameterization. Across channels, the family $\{q_c^{(n)}(t | x_c^{(n)})\}_{c=1}^C$ provides a parametric approximation to the event-time posteriors $\{p_c^{(n)}(t)\}_{c=1}^C$ introduced in the problem formulation, and jointly defines the EPDE-induced posterior $q_\phi(T^{(n)} | X^{(n)})$ over latent event times $T^{(n)} = \{T_c^{(n)}\}_{c=1}^C$ used in the variational objective. The predicted next-event times $\tilde{t}_{c,k}^{(n)}$ then serve as mean parameters for the mean-evolving lognormal mechanism (MELP) that models stochastic variability in event timing, as detailed in the next subsection.

4.5. Sampling: Mean-Evolving Lognormal Process (MELP)

For each sequence $X^{(n)}$ and channel c , given the previous event time $\tilde{t}_{c,i-1}^{(n)}$, the EPDE produces a K -dimensional vector of *candidate mean intervals* $\tilde{\tau}_c^{(n)} = (\tilde{\tau}_{c,1}^{(n)}, \dots, \tilde{\tau}_{c,K}^{(n)}) \in \mathbb{R}_+^K$, together with mixture weights $\mathbf{w}_c^{(n)} = (w_{c,1}^{(n)}, \dots, w_{c,K}^{(n)}) \in \Delta^{K-1}$ and scales $\mathbf{s}_c^{(n)} = (s_{c,1}^{(n)}, \dots, s_{c,K}^{(n)}) \in \mathbb{R}_+^K$. MELP draws the inter-event interval $\tau_{c,i}^{(n)}$ from a lognormal mixture:

$$p(\tau_{c,i}^{(n)} | \tilde{t}_{c,i-1}^{(n)}, X^{(n)}) = \sum_{j=1}^K w_{c,j}^{(n)} \text{LogN}(\tau_{c,i}^{(n)}; \mu_{c,j}^{(n)}, (s_{c,j}^{(n)})^2), \quad (18)$$

where $\text{LogN}(\cdot; \mu, s^2)$ denotes a lognormal density with log-mean μ and log-variance s^2 .

For each component j , we choose $\mu_{c,j}^{(n)}$ as a function of $\tilde{\tau}_{c,j}^{(n)}$ and $s_{c,j}^{(n)}$ so that the *mean* of the corresponding lognormal distribution matches the EPDE-predicted interval $\tilde{\tau}_{c,j}^{(n)}$. This ties the mixture components' average inter-event times directly to the EPDE outputs, while the scales $s_{c,j}^{(n)}$ control uncertainty around these means.

Sampling from MELP is reparameterized to keep gradients pathwise:

$$\begin{aligned} k &\sim \text{Cat}(\mathbf{w}_c^{(n)}), & \varepsilon &\sim \mathcal{N}(0, 1), \\ \tau_{c,i}^{(n)} &= \exp(\mu_{c,k}^{(n)} + s_{c,k}^{(n)} \varepsilon), & t_{c,i}^{(n)} &= t_{c,i-1}^{(n)} + \tau_{c,i}^{(n)}. \end{aligned} \quad (19)$$

$$(20)$$

During training we use a differentiable variant of (19) (e.g., Gumbel-Softmax) and take hard samples at test

time. MELP guarantees positive inter-event intervals, captures multimodal timing statistics, and yields closed-form component-wise KL terms against a lognormal(-mixture) prior in the learning objective. Moreover, the mixture expectation $\mathbb{E}[\tau_{c,i}^{(n)}] = \sum_{j=1}^K w_{c,j}^{(n)} \tilde{\tau}_{c,j}^{(n)}$ is available in closed form and is used in downstream computations such as computing ERG lags.

4.6. Event-relational graph (ERG)

For each sequence n , we infer an event-driven graph with adjacency $A^{(n)}(t) \in [0, 1]^{C \times C}$ conditioned on the EPDE-MELP event posterior $q_\phi(T^{(n)} | X^{(n)})$, where $T^{(n)} = \{T_c^{(n)}\}_{c=1}^C$ and $T_c^{(n)} = \{t_{c,k}^{(n)}\}_{k=1}^{K_c^{(n)}}$. Given a latent event realization $T \sim q_\phi(T^{(n)} | X^{(n)})$ and time t , let $\tilde{t}_c^{(n)}(t; T) := \max\{t_{c,k}^{(n)} \leq t\}$ denote the most recent event time on channel c up to t (set $\tilde{t}_c^{(n)}(t; T) = 0$ if none). We define the signed lag $\Delta \tilde{t}_{ij}^{(n)}(t; T) := \tilde{t}_i^{(n)}(t; T) - \tilde{t}_j^{(n)}(t; T)$, and map it to an edge score via a smooth function $\varphi_\eta : \mathbb{R} \rightarrow [0, 1]$ (STDP-shaped in our implementation, e.g., $\varphi_\eta(x) = \exp(-\alpha|x|)$ with $\eta = \{\alpha\}$):

$$e_{ij}^{(n)}(t; T) = \varphi_\eta(\Delta \tilde{t}_{ij}^{(n)}(t; T)) \in [0, 1]. \quad (21)$$

We approximate the posterior edge weight with S_{MC} Monte Carlo samples $\{T^{(n,s)}\}_{s=1}^{S_{MC}}$:

$$\bar{A}_{ij}^{(n)}(t) = \frac{1}{S_{MC}} \sum_{s=1}^{S_{MC}} \varphi_\eta(\Delta \tilde{t}_{ij}^{(n)}(t; T^{(n,s)})), \quad (22)$$

$$\bar{A}_{ij}^{(n)} = \frac{1}{M} \sum_{m=1}^M \bar{A}_{ij}^{(n)}(t_m), \quad (23)$$

where $\{t_m\}_{m=1}^M$ is a fixed time grid in the window (used to obtain a single adjacency $\bar{A}^{(n)}$ for downstream graph layers). We set $\bar{A}_{ii}^{(n)} = 0$ and optionally symmetrize for undirected GNNs.

To weakly align ERG connectivity with an observable statistic from $X^{(n)}$ (e.g., Pearson correlation $s_{ij}^{(n)} \in (-1, 1)$), we use Fisher- z matching:

$$z_{ij}^{\text{obs},(n)} = \text{atanh}(s_{ij}^{(n)}), \quad z_{ij}^{\text{pred},(n)} = \text{atanh}(2\bar{A}_{ij}^{(n)} - 1), \quad (24)$$

and define the ERG regularizer

$$\mathcal{R}_{\text{ERG}}^{(n)} = \sum_{i < j} \left[\frac{(z_{ij}^{\text{obs},(n)} - z_{ij}^{\text{pred},(n)})^2}{2\sigma^2} + \frac{1}{2} \log \sigma^2 \right], \quad (25)$$

where $\sigma > 0$ is fixed or learned and the term is weighted by β in the overall objective.

The implementation details and additional theoretical results are provided in Appendix F and A, respectively.

5. Experiments

In our experimental evaluations, we rigorously assessed the performance of LERD across synthetic benchmarks and real Alzheimer’s disease (AD) EEG datasets. First, we validated LERD using synthetic event-sequence data, demonstrating its effectiveness in accurately inferring latent event dynamics compared to baseline neural ODE models. Subsequently, we conducted comprehensive experiments on two diverse EEG datasets (AD cohorts A and B), covering Alzheimer’s disease, frontotemporal dementia, mild cognitive impairment, and healthy controls.

Table 1. Toy dataset results by frequency band. CS: Cosine Similarity, IoU: Intersection-over-Union.

Freq Band (Hz)	Model	CS	Median Rate	95% CI	IoU
[5, 10]	NODE	0.951	1.000	[1.000, 1.000]	0.000
[5, 10]	ODE-RNN	0.951	1.000	[1.000, 1.000]	0.000
[5, 10]	STRODE	0.967	0.340	[0.269, 0.410]	0.000
[5, 10]	LERD (Ours)	0.983	7.532	[4.300, 14.867]	0.473
[10, 15]	NODE	0.951	1.000	[1.000, 1.000]	0.000
[10, 15]	ODE-RNN	0.951	1.000	[1.000, 1.000]	0.000
[10, 15]	STRODE	0.964	0.251	[0.153, 0.348]	0.000
[10, 15]	LERD (Ours)	0.982	12.503	[7.587, 24.918]	0.289
[15, 20]	NODE	0.951	1.000	[1.000, 1.000]	0.000
[15, 20]	ODE-RNN	0.951	1.000	[1.000, 1.000]	0.000
[15, 20]	STRODE	0.961	0.532	[0.369, 0.695]	0.000
[15, 20]	LERD (Ours)	0.976	18.843	[10.465, 35.244]	0.202

5.1. Toy Dataset

The toy dataset experiments evaluated how well LERD and baseline neural ODE methods (NODE (Chen et al., 2018), ODE-RNN (Habiba & Pearlmutter, 2020), and STRODE (Huang et al., 2021)) recover latent event dynamics across distinct frequency bands ([5–10], [10–15], and [15–20] Hz). As summarized in Table 1, baseline methods achieved strong cosine similarity (CS) scores across all frequency bands, reflecting good sequence-level prediction performance. However, their intersection-over-union (IoU) scores were uniformly zero, indicating a fundamental limitation in capturing the latent event structure. This outcome highlights the common issue with purely data-driven neural approaches: despite excellent predictive accuracy, they often fail to recover the underlying generative mechanisms of data.

In contrast, LERD maintained similarly high CS scores while notably achieving meaningful IoU values (e.g., 0.473 at [5–10] Hz, 0.289 at [10–15] Hz, and 0.202 at [15–20] Hz). These non-zero IoU scores demonstrate that LERD captures latent structures consistent with the generative process and that its event-rate latents track the underlying oscillatory structure rather than acting as arbitrary embeddings. Moreover, the predicted event rates from LERD showed wider but informative uncertainty intervals, aligning closely with the true frequency band intervals. Such uncertainty quantification highlights LERD’s capacity to provide both accurate predictions and useful latent summaries in noisy and am-

biguous settings. Additional data generation protocols are provided in Appendix E.

5.2. Alzheimer’s Disease EEG Dataset

We extensively evaluated LERD on two diverse EEG datasets covering Alzheimer’s disease (AD), frontotemporal dementia (FTD), mild cognitive impairment (MCI), and healthy controls, as shown in Table 2. Across both datasets, LERD outperformed state-of-the-art baselines such as CNNs, RNNs, and transformers. In Dataset AD cohort A, LERD showed a clear ability to distinguish AD, FTD, and healthy participants, with consistently lower performance variability across runs. This stability highlights its effectiveness in capturing subtle neural dynamics despite EEG heterogeneity. In the more unbalanced Dataset AD cohort B, where distinctions between moderate AD, MCI, and healthy controls are subtler, LERD still achieved the highest diagnostic accuracy. While some baselines showed significant performance fluctuations, LERD remained robust, balancing sensitivity and specificity—demonstrating resilience to noise and distribution shifts common in real-world EEG data. Overall, LERD yields physiology-aligned latent summaries alongside strong predictive performance, supporting analyses of group-level spectral/connectivity differences under a strict cross-subject protocol. Additional dataset descriptions and baseline methods are presented in Appendix E.

Table 2. Results on Alzheimer’s EEG datasets (mean ± std).

Model	Dataset AD cohort A		Dataset AD cohort B	
	Accuracy (%)	F1 (%)	Accuracy (%)	F1 (%)
EEGNet	68.10 ± 7.10	66.49 ± 12.33	71.37 ± 26.02	60.85 ± 26.93
LCADNet	70.52 ± 5.09	68.12 ± 7.69	72.44 ± 24.16	49.38 ± 15.84
LSTM	70.52 ± 8.68	68.24 ± 9.59	77.89 ± 9.91	61.35 ± 20.35
ATCNet	64.71 ± 6.80	60.98 ± 4.55	71.09 ± 32.50	50.92 ± 23.61
ADFormer	69.35 ± 6.61	65.28 ± 7.87	82.38 ± 14.71	63.89 ± 12.09
LEAD	72.68 ± 4.57	69.98 ± 9.61	80.00 ± 15.55	62.21 ± 14.82
LERD	75.03 ± 8.29	72.69 ± 8.16	89.82 ± 8.39	64.87 ± 10.67

5.3. Experimental Setup

We evaluate LERD under a five-fold cross-subject protocol to ensure that generalization is assessed on previously unseen participants rather than unseen windows from the same individuals. For each cohort, subjects are partitioned into five disjoint folds with stratification at the subject level so that the class proportions of Alzheimer’s disease, frontotemporal dementia/mild cognitive impairment, and healthy controls are approximately preserved in every split. In each round, four folds are used for training, and one for testing; the roles of the folds are rotated until every fold serves exactly once in the held-out test set.

EEG is segmented into non-overlapping two-second windows (1,000 samples at 500 Hz) per subject and channel, followed by channel-wise z-normalization computed within

Table 3. Ablation of spike-informed and connectome priors in LERD on Alzheimer’s EEG Datasets. Accuracy and F1 (%) reported as mean ± std.

Dataset	Variant	Accuracy (%)	F1 (%)
AD cohort A	No prior	70.52 ± 11.83	65.46 ± 13.10
	dLIF prior	73.92 ± 9.84	71.41 ± 10.72
	ERG prior	72.75 ± 6.63	70.35 ± 7.91
	Dual priors	75.03 ± 8.29	72.69 ± 8.16
AD cohort B	No prior	83.22 ± 15.10	60.72 ± 12.37
	dLIF prior	87.98 ± 8.09	62.95 ± 9.24
	ERG prior	86.20 ± 9.96	65.63 ± 9.17
	Dual priors	89.82 ± 8.39	64.87 ± 10.67

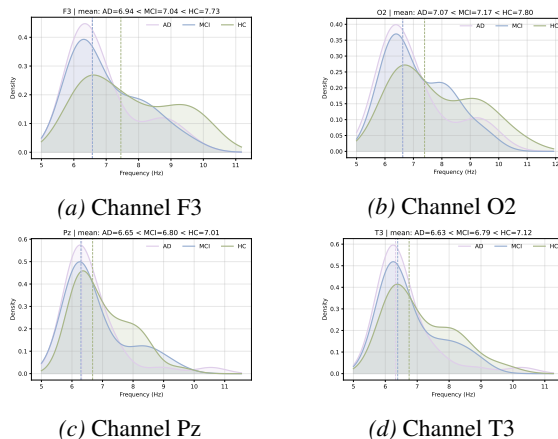


Figure 2. Kernel density estimates of the inferred dLIF frequency distributions across Alzheimer’s disease (AD), mild cognitive impairment (MCI), and healthy control (HC) groups for EEG channels F3, O2, Pz, and T3. The decreasing central frequency with increasing disease severity is consistent with established AD EEG slowing and serves as a model-derived latent summary.

the training portion of the active fold and then applied to validation and test windows of that fold.

Evaluation is conducted at subject levels. Subject-level predictions aggregate a subject’s windows by majority vote over window-wise labels. We report accuracy, macro-F1, and summarize performance as the mean and standard deviation across the five test folds.

5.4. Ablation Studies

We ablated LERD to assess each prior’s impact on predictive performance (Table 3). On AD Cohort A, the no-prior baseline is moderate; adding the dLIF prior boosts accuracy, while the ERG prior improves accuracy and F1 via inter-channel modeling. Combining both yields the best scores. On AD Cohort B, the pattern holds with larger gains: the dLIF prior gives the biggest accuracy lift under subtler classes, and the ERG prior raises F1. Their combination again performs best. Overall, each prior helps, and together they provide robust predictions on realistic EEG.

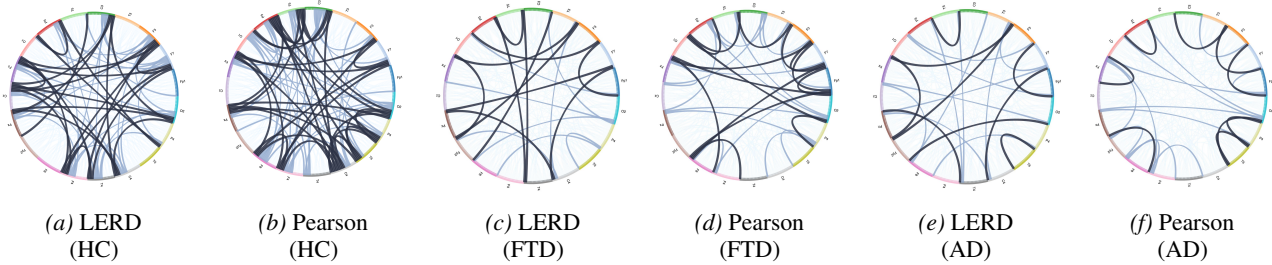


Figure 3. Comparison of EEG connectivity graphs inferred by LERD versus Pearson correlation-based priors across healthy controls (HC), frontotemporal dementia (FTD), and Alzheimer’s disease (AD) groups.

6. Visualizations

Our visualizations present *model-derived latent summaries* that are commonly analyzed in EEG studies (e.g., frequency shifts and connectivity changes), but now obtained from the LERD latent event/graph variables. Specifically, we show (i) inferred frequency distributions from the dLIF-constrained latent rate dynamics across key EEG channels, (ii) event-relational graphs compared to correlation-based connectivity, and (iii) boundary-time recovery on a synthetic dataset with ground truth.

6.1. dLIF Inferred Frequency Visualization

To further analyze the latent neural dynamics captured by LERD, we visualized the inferred frequency distributions derived from the differentiable leaky-integrate-and-fire (dLIF) prior across several key EEG channels associated with Alzheimer’s disease progression, including channels F3, O2, Pz, and T3. Figure 2a exemplifies the frequency distributions at channel F3 for the Alzheimer’s disease (AD), mild cognitive impairment (MCI), and healthy control (HC) groups. The distributions illustrate a trend of decreasing frequency with increasing disease severity. Specifically, healthy controls exhibit the highest central frequency, indicating typical neural oscillatory activity. Subjects with MCI show slightly reduced frequency values, signifying the onset of neural slowing, while the AD group displays the lowest central frequencies, reflecting neural slowing commonly reported in Alzheimer’s pathology. This consistent pattern across multiple channels indicates that the learned latent rate variables align with established EEG band-shift phenomena and can support group-level analyses.

6.2. Graph Connectivity Visualization

We also visualized LERD’s inferred event-relational graphs (ERGs) against Pearson correlation-based connectivity graphs (Figure 3). Chord diagrams revealed distinct connectivity patterns across healthy controls (HC), FTD, and AD groups. LERD’s ERGs captured trends consistent with prior dementia EEG findings: HC showed denser connectiv-

ity, while FTD and AD exhibited sparser and weaker links. Some similarity to Pearson graphs is expected because we include a weak Fisher- z alignment term that encourages (but does not enforce) agreement with correlation-based summaries. Overall, the ERG provides a timing-derived connectivity summary that can be compared alongside standard measures.

6.3. Boundary Time Prediction Visualization

Figure 4 visually compares the predicted versus ground-truth boundary times for STRODE and LERD across three distinct frequency bands ([5–10 Hz], [10–15 Hz], and [15–20 Hz]). STRODE demonstrates noticeable deviations from the ideal diagonal alignment, suggesting challenges in accurately recovering true boundary timings, particularly at higher frequency bands. In contrast, LERD consistently maintains a tighter diagonal alignment across all frequency ranges, indicating superior accuracy and robustness in capturing underlying temporal structures. This visualization clearly illustrates LERD’s effectiveness in accurately inferring latent event boundaries in the toy dataset, reinforcing its suitability for precise temporal modeling in EEG data.

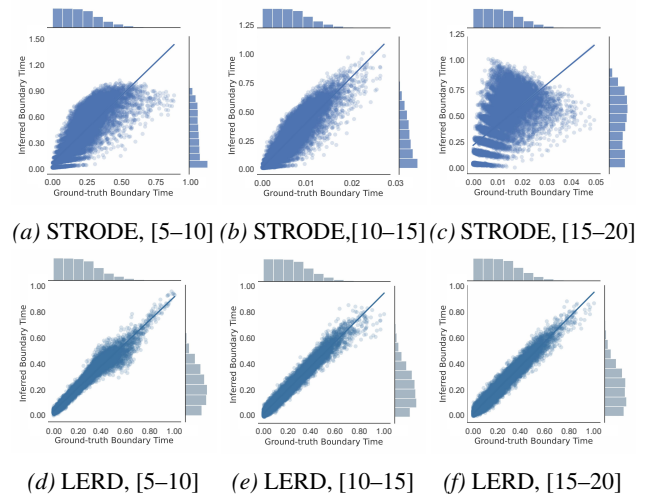


Figure 4. Predicted vs. ground-truth boundary times across frequency bands ([5–10], [10–15], [15–20] Hz): STRODE vs. LERD.

7. Conclusion

We presented LERD, a Bayesian electrophysiological neural dynamical system that infers latent event dynamics and a conditional event-relational graph directly from multi-channel EEG. By coupling an Event Posterior Differential Equation (EPDE) with a Mean-Evolving Lognormal Process (MELP) and an electrophysiology-inspired dLIF prior, the model yields physiology-aligned latent variables and supports end-to-end prediction. Our theory provides a tractable IVP-based upper bound for the event-prior KL and establishes stability of the inferred graph to lag noise, while experiments on synthetic and AD EEG data demonstrate superior accuracy and model-derived latent summaries that can support downstream scientific analyses.

Impact Statement

This paper presents work whose goal is to advance the field of machine learning for modeling and classifying neurodegenerative disease from EEG. If deployed responsibly, such models could support earlier screening and improve understanding of disease-related electrophysiological dynamics.

Potential negative impacts include misuse as a standalone diagnostic tool, leading to false positives/negatives and downstream harm; reduced performance under dataset shift (different sites, devices, demographics, or protocols); and privacy risks because EEG is sensitive health data. To mitigate these risks, we emphasize that LERD is intended as a research and decision-support model rather than a replacement for clinical judgment, and that any real-world use should include rigorous external validation, fairness and subgroup analyses, uncertainty reporting, and strong data governance (consent, de-identification, and secure storage).

References

Acharya, M., Deo, R. C., Tao, X., Barua, P. D., Devi, A., Atmakuru, A., and Tan, R. Deep learning techniques for automated Alzheimer’s and mild cognitive impairment disease using EEG signals: A comprehensive review of the last decade (2013–2024). *Computer Methods and Programs in Biomedicine*, 259:108506, 2025. doi: 10.1016/j.cmpb.2024.108506.

Altaheri, H., Muhammad, G., and Alsulaiman, M. Physics-informed attention temporal convolutional network for eeg-based motor imagery classification. *IEEE transactions on industrial informatics*, 19(2):2249–2258, 2022.

Babiloni, C. et al. International federation of clinical neurophysiology (ifcn) recommendations on electroencephalography in Alzheimer’s disease and other dementias. *Clinical Neurophysiology*, 2021.

Bastos, A. M. and Schoffelen, J.-M. A tutorial review of functional connectivity analysis methods and their interpretational pitfalls. *Frontiers in Systems Neuroscience*, 9:175, 2016. doi: 10.3389/fnsys.2015.00175.

Bi, G. Q. and Poo, M.-M. Synaptic modifications in cultured hippocampal neurons: dependence on spike timing, synaptic strength, and postsynaptic cell type. *The Journal of Neuroscience*, 18(24):10464–10472, 1998. doi: 10.1523/JNEUROSCI.18-24-10464.1998.

Burkitt, A. N. A review of the integrate-and-fire neuron model: I. homogeneous synaptic input. *Biological Cybernetics*, 95(1):1–19, 2006. doi: 10.1007/s00422-006-0068-6.

Chen, R. T., Rubanova, Y., Bettencourt, J., and Duvenaud, D. K. Neural ordinary differential equations. *Advances in neural information processing systems*, 31, 2018.

Dauwels, J., Vialatte, F., and Cichocki, A. A comparative study of synchrony measures for the early diagnosis of Alzheimer’s disease based on eeg. *Clinical Neurophysiology*, 121(1):81–94, 2010.

Ehteshamzad, M. et al. Assessing the potential of EEG in early detection of Alzheimer’s disease. *Alzheimer’s & Dementia: Diagnosis, Assessment & Disease Monitoring*, 2024. doi: 10.3233/ADR-230159.

Feldman, D. E. The spike-timing dependence of plasticity. *Neuron*, 75(4):556–571, 2012. doi: 10.1016/j.neuron.2012.08.001.

Habiba, M. and Pearlmutter, B. A. Neural ordinary differential equation based recurrent neural network model. In *2020 31st Irish signals and systems conference (ISSC)*, pp. 1–6. IEEE, 2020.

Huang, H., Liu, H., Wang, H., Xiao, C., and Wang, Y. Strobe: Stochastic boundary ordinary differential equation. In *International Conference on Machine Learning*, pp. 4435–4445. PMLR, 2021.

Hunyadi, B., Woolrich, M. W., Quinn, A. J., Vidaurre, D., and De Vos, M. A dynamic system of brain networks revealed by fast transient eeg fluctuations and their fmri correlates. *NeuroImage*, 185:72–82, 2019. doi: 10.1016/j.neuroimage.2018.09.082.

Ieracitano, C., Mammone, N., Hussain, A., and Morabito, F. C. A novel multi-modal machine learning based approach for automatic classification of eeg recordings in dementia. *Neural Networks*, 123:176–190, 2020. doi: 10.1016/j.neunet.2019.12.006.

Jeong, J. Eeg dynamics in patients with alzheimer’s disease. *Clinical Neurophysiology*, 115(7):1490–1505, 2004. doi: 10.1016/j.clinph.2004.01.001.

- Kachare, P., Puri, D., Sangle, S. B., Al-Shourbaji, I., Jabbari, A., Kirner, R., Alameen, A., Migdady, H., and Abualigah, L. Lcadnet: a novel light cnn architecture for eeg-based alzheimer disease detection. *Physical and Engineering Sciences in Medicine*, 47(3):1037–1050, 2024.
- Kiebel, S. J., Garrido, M. I., Moran, R., Chen, C.-C., and Friston, K. J. Dynamic causal modeling for eeg and meg. *Human Brain Mapping*, 30(6):1866–1876, 2009. doi: 10.1002/hbm.20775.
- Kim, S.-K., Kim, H., Kim, S. H., Kim, J. B., and Kim, L. Electroencephalography-based classification of alzheimer’s disease spectrum during computer-based cognitive testing. *Scientific Reports*, 14, 2024. doi: 10.1038/s41598-024-55656-8.
- Klepl, D., Wu, M., and He, F. Graph neural network-based EEG classification: A survey. *IEEE Transactions on Neural Systems and Rehabilitation Engineering*, 32:493–503, 2024. doi: 10.1109/TNSRE.2024.3355750.
- Lawhern, V. J., Solon, A. J., Waytowich, N. R., Gordon, S. M., Hung, C. P., and Lance, B. J. Eegnet: a compact convolutional neural network for eeg-based brain-computer interfaces. *Journal of neural engineering*, 15(5):056013, 2018.
- Mahjoory, K., Nikulin, V. V., Botrel, L., Linkenkaer-Hansen, K., Fato, M. M., and Haufe, S. Consistency of EEG source localization and connectivity estimates. *NeuroImage*, 152:590–601, 2017. doi: 10.1016/j.neuroimage.2017.02.076.
- Michel, C. M. and Brunet, D. EEG source imaging: A practical review of the analysis steps. *Frontiers in Neurology*, 10:325, 2019. doi: 10.3389/fneur.2019.00325.
- Michel, C. M. and Koenig, T. Eeg microstates as a tool for studying the temporal dynamics of whole-brain neuronal networks: A review. *NeuroImage*, 180:577–593, 2018. doi: 10.1016/j.neuroimage.2017.11.062.
- Michel, C. M., Murray, M. M., Lantz, G., Gonzalez Andino, S., Spinelli, L., and Grave de Peralta Menendez, R. EEG source imaging. *Clinical Neurophysiology*, 115(10):2195–2222, 2004. doi: 10.1016/j.clinph.2004.06.001.
- Miltiadous, A., Tzimourta, K. D., Afrantou, T., Ioannidis, P., Grigoriadis, N., Tsalikakis, D. G., Angelidis, P., Tsiouras, M. G., Glavas, E., Giannakeas, N., and Tzallas, A. T. ”a dataset of eeg recordings from: Alzheimer’s disease, frontotemporal dementia and healthy subjects”, 2024.
- Neftci, E. O., Mostafa, H., and Zenke, F. Surrogate gradient learning in spiking neural networks: Bringing the power of gradient-based optimization to spiking neural networks. *IEEE Signal Processing Magazine*, 36(6):61–74, 2019.
- Pineda, A. M., Ramos, F. M., Betting, L. E., and Campanharo, A. S. L. O. Use of complex networks for the automatic detection and the diagnosis of Alzheimer’s disease. In Rojas, I., Joya, G., and Catala, A. (eds.), *Advances in Computational Intelligence: 15th International Work-Conference on Artificial Neural Networks (IWANN 2019), Proceedings, Part I*, volume 11506 of *Lecture Notes in Computer Science*, pp. 115–126, Cham, 2019. Springer. doi: 10.1007/978-3-030-20521-8_10.
- Sadegh-Zadeh, S.-A., Fakhri, E., Bahrami, M., Bagheri, E., Khamsehashari, R., Noroozian, M., and Hajiyavand, A. M. An approach toward artificial intelligence alzheimer’s disease diagnosis using brain signals. *diagnostics*, 13(3):477, 2023.
- Tawhid, M. N. A., Siuly, S., Kabir, E., and Li, Y. Advancing alzheimer’s disease detection: a novel convolutional neural network based framework leveraging eeg data and segment length analysis. *Brain Informatics*, 12(1):13, 2025. doi: 10.1186/s40708-025-00260-3. URL <https://braininformatics.springeropen.com/articles/10.1186/s40708-025-00260-3>.
- Vicchietti, M. L., Ramos, F. M., Betting, L. E., and Campanharo, A. S. L. O. Computational methods of eeg signals analysis for Alzheimer’s disease classification. *Scientific Reports*, 13:8184, 2023. doi: 10.1038/s41598-023-32664-8.
- Wang, Y., Mammone, N., Petrovsky, D., Tzallas, A. T., Morabito, F. C., and Zhang, X. ADformer: A multi-granularity transformer for EEG-based Alzheimer’s disease assessment. arXiv preprint arXiv:2409.00032, 2024.
- Wang, Y., Huang, N., Mammone, N., Cecchi, M., and Zhang, X. Lead: Large foundation model for eeg-based alzheimer’s disease detection. *arXiv preprint arXiv:2502.01678*, 2025.
- Zhang, X. and Yao, L. *Deep learning for EEG-based brain-computer interfaces: representations, algorithms and applications*. World Scientific, 2021.

A. Theory

We analyze how entry-wise perturbations of lags affect the learned ERG when the edge map is exponential. For channels $i \neq j$ and time t , let the noise-free lag be $\Delta t_{ij}(t; T)$ and the perturbed lag be $\widetilde{\Delta} t_{ij}(t; T) = \Delta t_{ij}(t; T) + \xi_{ij}(t; T)$. Define the edge map $\phi_\alpha(x) = \exp(-\alpha|x|) \in [0, 1]$ with slope parameter $\alpha > 0$ and the (noise-free and perturbed) edges

$$e_{ij}(t; T) = \phi_\alpha(\Delta t_{ij}(t; T)), \quad \widetilde{e}_{ij}(t; T) = \phi_\alpha(\widetilde{\Delta} t_{ij}(t; T)).$$

The decoder uses the Monte-Carlo, time-averaged adjacencies

$$\bar{A}_{ij} = \frac{1}{MS} \sum_{m=1}^M \sum_{s=1}^S e_{ij}(t_m; T^{(s)}),$$

$$\widetilde{\bar{A}}_{ij} = \frac{1}{MS} \sum_{m=1}^M \sum_{s=1}^S \widetilde{e}_{ij}(t_m; T^{(s)}).$$

Theorem A.1 (Entry-wise and matrix stability). *The exponential edge map is globally α -Lipschitz: for all $x, y \in \mathbb{R}$,*

$$|\phi_\alpha(x) - \phi_\alpha(y)| \leq \alpha |x - y|. \quad (26)$$

Consequently, for any (i, j, t, T) ,

$$|\widetilde{e}_{ij}(t; T) - e_{ij}(t; T)| \leq \alpha |\xi_{ij}(t; T)|. \quad (27)$$

Averaging over time and Monte-Carlo samples yields the entry-wise bound

$$|\widetilde{\bar{A}}_{ij} - \bar{A}_{ij}| \leq \alpha \overline{|\xi_{ij}|}, \quad \overline{|\xi_{ij}|} := \frac{1}{MS} \sum_{m=1}^M \sum_{s=1}^S |\xi_{ij}(t_m; T^{(s)})|, \quad (28)$$

and the matrix (Frobenius-norm) bound

$$\|\widetilde{\bar{A}} - \bar{A}\|_F \leq \frac{\alpha}{MS} \sum_{m=1}^M \sum_{s=1}^S \|\Xi^{(m,s)}\|_F, \quad \Xi^{(m,s)} := [\xi_{ij}(t_m; T^{(s)})]_{i \neq j}, \quad (29)$$

hence $\|\widetilde{\bar{A}} - \bar{A}\|_F \leq \alpha \overline{\|\Xi\|_F}$ with $\overline{\|\Xi\|_F}$ the average Frobenius norm of lag-noise matrices.

Corollary A.2 (Deterministic and probabilistic perturbation bounds). (i) (Uniformly bounded noise). *If $|\xi_{ij}(t; T)| \leq \varepsilon_\infty$ almost surely, then*

$$|\widetilde{\bar{A}}_{ij} - \bar{A}_{ij}| \leq \alpha \varepsilon_\infty, \quad \|\widetilde{\bar{A}} - \bar{A}\|_F \leq \alpha \varepsilon_\infty \sqrt{C(C-1)}. \quad (30)$$

(ii) (Sub-Gaussian noise). *Suppose $\{\xi_{ij}(t_m; T^{(s)})\}_{m,s}$ are i.i.d., mean-zero, sub-Gaussian with proxy σ^2 (i.e., $\mathbb{E}e^{\lambda\xi} \leq \exp(\lambda^2\sigma^2/2)$). Then each difference $\Delta_{ij} := \widetilde{\bar{A}}_{ij} - \bar{A}_{ij}$ is sub-Gaussian with proxy $\alpha^2\sigma^2/(MS)$ and*

$$\mathbb{P}(|\Delta_{ij}| \geq \tau) \leq 2 \exp\left(-\frac{MS\tau^2}{2\alpha^2\sigma^2}\right). \quad (31)$$

If, in addition, $\xi \sim \mathcal{N}(0, \sigma^2)$, then

$$\mathbb{E}[|\Delta_{ij}|] \leq \alpha\sigma\sqrt{\frac{2}{\pi}}, \quad \mathbb{E}[\|\widetilde{\bar{A}} - \bar{A}\|_F] \leq \alpha\sigma\sqrt{\frac{2}{\pi}}\sqrt{C(C-1)}. \quad (32)$$

Implication. Small perturbations in EPDE/MELP lags translate linearly (in α) to entry-wise changes in the ERG, and averaging over samples/time further contracts the perturbation. Thus the ERG is provably stable to modest timing noise, with explicit constants controlled by the edge map slope α and the noise magnitude.

B. Proof of Theorem 4.1

Here, we first present the Lemma that support the proof of Theorem 4.1.

Lemma B.1 (Shift–stability of IVPs (Huang et al., 2021)). *Let $e > 0$ and $U \subset \mathbb{R}^n$ be open. Let $f_1, f_2 : [a - 2e, a] \rightarrow \mathbb{R}^n$ be continuously differentiable with $\|f_1'\| \leq M$ for some $M > 0$. Consider*

$$y_1'(t) = f_1(t), \quad y_1(a - e) = x_1, \quad y_2'(t) = f_2(t) = f_1(t - e), \quad y_2(a - e) = x_2.$$

Then, as $e \rightarrow 0^+$,

$$\lim_{e \rightarrow 0^+} \left(\lim_{t \rightarrow a} \|y_1(t) - y_2(t)\| \right) \leq \lim_{e \rightarrow 0^+} \|x_1 - x_2\|.$$

Proof. By definition,

$$\text{KL}(q\|p_r) = \int_0^S q(t) \log \frac{q(t)}{r(t)e^{-\int_0^t r}} dt.$$

Using $m = -e^{-t}$, we have $t = -\log(-m) = M$ and $dt = -\frac{1}{m} dm$. Hence

$$\text{KL}(q\|p_r) = \int_{-e^{-S}}^0 \frac{q(M)}{M} \log \frac{q(M)}{Mr(M)e^{-\int_0^M r}} \left(-\frac{1}{m}\right) dm = \int_{-e^{-S}}^0 g(m) dm.$$

This improper integral equals $\lim_{\varepsilon \downarrow 0} \int_{-e^{-S}}^{-\varepsilon} g(m) dm = \lim_{\varepsilon \downarrow 0} G(-\varepsilon)$, proving Eq. (10). Since $r(t) \in [a, b]$ and q is integrable, g is locally integrable near $m = 0^-$. Split the integral at $-\varepsilon$ and at -2ε :

$$\int_{-e^{-S}}^0 g = \int_{-e^{-S}}^{-\varepsilon} g + \int_{-\varepsilon}^0 g \leq G(-\varepsilon) + \left| \int_{-\varepsilon}^0 g \right| \leq G(-\varepsilon) + \left| \int_{-2\varepsilon}^{-\varepsilon} g \right| = G(-\varepsilon) + |G(-2\varepsilon) - G(-\varepsilon)|,$$

which yields Eq. (11). The last inequality uses Lemma B.1 (applied to the IVPs $G_1'(m) = g(m)$ and $G_2'(m) = g(m)$ shifted by ε) to control the tail near the singular endpoint and the fact that r is bounded in $[a, b]$, ensuring g remains controlled as $m \rightarrow 0^-$. As $\varepsilon \downarrow 0$, the tail vanishes by dominated convergence, hence $\mathcal{U}_\varepsilon \rightarrow \text{KL}(q\|p_r)$. \square

C. Proof of Theorem A.1

Proof. (Lipschitzness). The absolute value is 1–Lipschitz: $\|x| - |y| \leq |x - y|$. The function $u \mapsto e^{-\alpha u}$ on $u \geq 0$ has derivative $|\alpha e^{-\alpha u}| \leq \alpha$, hence it is α –Lipschitz on $\mathbb{R}_{\geq 0}$. By composition of Lipschitz maps,

$$|\phi_\alpha(x) - \phi_\alpha(y)| = |e^{-\alpha|x|} - e^{-\alpha|y|}| \leq \alpha ||x| - |y|| \leq \alpha |x - y|,$$

establishing Eq. (26). Taking $y = x + \xi$ gives Eq. (27).

(Averaging). Using linearity of the average and triangle inequality,

$$|\tilde{A}_{ij} - \bar{A}_{ij}| = \left| \frac{1}{MS} \sum_{m,s} (\tilde{e}_{ij}(t_m; T^{(s)}) - e_{ij}(t_m; T^{(s)})) \right| \leq \frac{1}{MS} \sum_{m,s} |\tilde{e}_{ij} - e_{ij}| \leq \frac{\alpha}{MS} \sum_{m,s} |\xi_{ij}(t_m; T^{(s)})|,$$

which is Eq. (28).

(Matrix bound). Define $\Delta^{(m,s)} := [\tilde{e}_{ij}(t_m; T^{(s)}) - e_{ij}(t_m; T^{(s)})]_{i \neq j}$, so $\tilde{A} - \bar{A} = \frac{1}{MS} \sum_{m,s} \Delta^{(m,s)}$. By the triangle inequality of the Frobenius norm,

$$\|\tilde{A} - \bar{A}\|_F \leq \frac{1}{MS} \sum_{m,s} \|\Delta^{(m,s)}\|_F.$$

Entry–wise inequality Eq. 27 implies $\|\Delta^{(m,s)}\|_F \leq \alpha \|\Xi^{(m,s)}\|_F$, giving Eq. (29). \square

D. Proof of Corollary A.2

Proof. (i) From Eq. (28), $|\xi_{ij}| \leq \varepsilon_\infty$, giving the entry-wise claim. For the matrix bound, $\|\Xi^{(m,s)}\|_F \leq \varepsilon_\infty \sqrt{C(C-1)}$ for every (m, s) ; apply Eq. (29).

(ii) For each fixed (i, j) , define i.i.d. variables $Y_{m,s} := \tilde{e}_{ij}(t_m; T^{(s)}) - e_{ij}(t_m; T^{(s)})$. By Eq. (27), $Y_{m,s}$ is an α -Lipschitz transform of $\xi_{ij}(t_m; T^{(s)})$, hence $Y_{m,s}$ is sub-Gaussian with proxy $\alpha^2 \sigma^2$ (standard Lipschitz preservation of the ψ_2 -norm). Then $\Delta_{ij} = (MS)^{-1} \sum_{m,s} Y_{m,s}$ is sub-Gaussian with proxy $\alpha^2 \sigma^2 / (MS)$, yielding Eq. (31) via the Chernoff bound.

For the Gaussian-mean bound, use $|Y_{m,s}| \leq \alpha |\xi_{ij}(t_m; T^{(s)})|$ and linearity:

$$\mathbb{E}|\Delta_{ij}| \leq \frac{\alpha}{MS} \sum_{m,s} \mathbb{E}|\xi| = \alpha \mathbb{E}|\xi| = \alpha \sigma \sqrt{\frac{2}{\pi}},$$

where the last equality is the mean absolute value of a zero-mean Gaussian. Summing the entry-wise bounds in quadrature gives the Frobenius expectation in Eq. (32). \square

E. Additional Experimental Details

E.1. Alzheimer’s Disease EEG Baseline Methods

To rigorously evaluate our proposed method, we benchmarked it against several representative deep learning approaches commonly utilized for EEG analysis. These baselines include convolutional, recurrent, attention-based, and transformer-based models, each demonstrating distinct strengths for capturing various aspects of EEG signal patterns.

EEGNet (Lawhern et al., 2018) is a compact convolutional neural network initially developed for EEG-based brain-computer interfaces. It integrates depthwise and separable convolutions to effectively capture temporal, spatial, and frequency-specific characteristics in EEG data, making it a well-recognized lightweight yet powerful model in EEG classification tasks.

LCADNet (Kachare et al., 2024) is specifically tailored for Alzheimer’s disease detection from EEG data. Utilizing optimized convolutional structures designed for computational efficiency without sacrificing discriminative power, LCADNet achieves competitive performance in resource-limited environments, making it a strong baseline for EEG-based AD diagnosis.

LSTM (Zhang & Yao, 2021) embodies recurrent neural networks tailored for modeling temporal dependencies inherent in EEG signals. By maintaining and updating hidden states across sequences, LSTMs effectively capture long-term dynamics and temporal correlations, making them naturally suitable for sequential EEG analyses.

ATCNet (Altaheri et al., 2022) employs a physics-informed architecture combining temporal convolutions with attention mechanisms. Originally proposed for motor imagery EEG classification, it effectively captures both local temporal details and global dependencies, showcasing adaptability across various EEG applications.

ADformer (Wang et al., 2024) is a multi-granularity transformer specifically crafted for Alzheimer’s disease evaluation using EEG signals. It utilizes multi-scale attention mechanisms to concurrently model fine-grained and coarse-grained temporal information, setting a high-performance standard in EEG-based AD diagnostics.

LEAD (Wang et al., 2025) exemplifies the recent advancement toward large-scale foundation models in EEG analysis. Pre-trained extensively on vast EEG datasets and fine-tuned for Alzheimer’s disease detection, LEAD leverages transfer learning to provide robust, generalizable EEG representations, establishing a new benchmark in EEG-based clinical assessments.

E.2. Dataset Descriptions

E.2.1. TOY DATASET AND DATA GENERATION

Frequency bands and sampling. To systematically evaluate our model’s ability to capture latent event dynamics, we constructed synthetic datasets with clearly defined frequency bands. We generated latent event rates λ from truncated normal distributions centered at the midpoint of each target frequency band: low band [5–10 Hz] with $\lambda \sim \text{TruncNormal}(\mu = 7.5, \sigma = 1.0; [5, 10])$, middle band [10–15 Hz] with $\lambda \sim \text{TruncNormal}(\mu = 12.5, \sigma = 1.0; [10, 15])$, and high band [15–20 Hz] with $\lambda \sim \text{TruncNormal}(\mu = 17.5, \sigma = 1.0; [15, 20])$. This design ensures concentrated event-rate distributions within each band while avoiding frequencies outside the desired range.

Data scale and splitting strategy. For each frequency band, we independently generated three data splits: a training set with 150 distinct event rates, each having 50 sequences (7,500 sequences total); a validation set with 25 new event rates and 50 sequences per rate (1,250 sequences total); and a test set with an additional 25 new event rates, again with 50 sequences per rate (1,250 sequences total). Importantly, no overlap of event rates occurs across training, validation, and test splits to ensure proper evaluation of model generalization.

Sequence generation. Each synthetic sequence comprises 20 observations, constructed by sampling inter-event times Δt_i from an exponential distribution with parameter λ . The event timestamps t_i are obtained cumulatively by $t_i = \sum_{j=1}^i \Delta t_j$. Observations y_i are subsequently generated using the relationship:

$$y_i = \sin(t_i) + \eta_i, \quad \eta_i \sim \mathcal{N}(0, \sigma_\eta^2),$$

where the default noise level is $\sigma_\eta = 0.07$. Additional sensitivity analyses varied σ_η within $\{0.05, 0.10, 0.15\}$ to assess model robustness.

Evaluation methodology. Model performance was comprehensively evaluated using three criteria: (1) classification score (CS) assessing sequence-level predictive accuracy, (2) uncertainty calibration, quantified through the median and 95% confidence interval of the estimated event rate $\hat{\lambda}$, obtained via nonparametric resampling within each frequency band, and (3) structural fidelity, measured using intersection-over-union (IoU) between the predicted latent structure and the ground-truth event patterns.

E.2.2. ALZHEIMER’S DISEASE EEG DATASET

Dataset AD Cohort A (Miltiadous et al., 2024) consists of resting-state, eyes-closed EEG recordings from a total of 88 participants, categorized into 36 individuals diagnosed with Alzheimer’s disease (AD), 23 patients with frontotemporal dementia (FTD), and 29 healthy control subjects (HC). The EEG data were collected using 19 electrodes arranged according to the international 10–20 placement system. The recordings have a sampling rate of 500 Hz and an average duration ranging from approximately 12 to 14 minutes per subject. Provided in adherence to the Brain Imaging Data Structure (BIDS) standard, the dataset includes both raw and preprocessed EEG signals, enabling robust comparative analysis across different dementia subtypes.

Dataset AD Cohort B (Sadegh-Zadeh et al., 2023) includes resting-state EEG data from 168 participants, segmented into 59 moderate Alzheimer’s disease patients (AD), 7 individuals diagnosed with mild cognitive impairment (MCI), and 102 healthy controls (HC). EEG recordings were acquired using the standardized 10–20 electrode placement system, with data presented in MATLAB (.mat) format. Accompanying the EEG data are Mini-Mental State Examination (MMSE) scores, providing cognitive assessments for participants. This dataset is particularly tailored for the distinction of AD from MCI, thus serving as a valuable resource for investigations aimed at early Alzheimer’s disease diagnosis.

E.3. Computational cost

To contextualize runtime/complexity, we report a per-window estimate of floating point operations (FLOPs) and parameter counts for a single 2-s EEG window (19 channels, 500 Hz). While LERD is heavier than lightweight CNN backbones (e.g., EEGNet), it remains substantially smaller than transformer-based baselines.

Table 4. Approximate computational cost for one 2-s EEG window (19 channels, 500 Hz).

Model	FLOPs	Params
LERD	60.176M	3.103M
EEGNet	9.989M	1.232K
LCADNet	7.783M	151.302K
LSTM	114.82M	5.5K
ATCNet	328.74M	4.3K
ADFormer	3.636G	5.34M
LEAD	0.766G	3.33M

E.4. Additional evaluation metrics

For completeness, we report sensitivity, specificity, and AUC (mean \pm s.d. across the five cross-subject folds) for both cohorts.

Table 5. Sensitivity, specificity, and AUC on Dataset AD cohort A.

Model	Sensitivity	Specificity	AUC
EEGNet	0.6830 \pm 0.1050	0.8463 \pm 0.0355	0.7646 \pm 0.0695
ADFormer	0.7017 \pm 0.0833	0.8495 \pm 0.0366	0.7756 \pm 0.0597
LSTM	0.6756 \pm 0.0692	0.8426 \pm 0.0382	0.7591 \pm 0.0529
ATCNet	0.6844 \pm 0.0627	0.8350 \pm 0.0334	0.7597 \pm 0.0460
LEAD	0.7067 \pm 0.0498	0.8594 \pm 0.0216	0.7830 \pm 0.0343
LCADNet	0.7006 \pm 0.0491	0.8445 \pm 0.0358	0.8462 \pm 0.0495
LERD	0.7493 \pm 0.0841	0.8793 \pm 0.0377	0.8143 \pm 0.0603

Table 6. Sensitivity, specificity, and AUC on Dataset AD cohort B.

Model	Sensitivity	Specificity	AUC
EEGNet	0.5544 \pm 0.0801	0.8717 \pm 0.0921	0.9494 \pm 0.0445
ADFormer	0.6249 \pm 0.0430	0.9546 \pm 0.0306	0.9714 \pm 0.0381
LSTM	0.5167 \pm 0.0867	0.9038 \pm 0.0387	0.9486 \pm 0.0314
ATCNet	0.6412 \pm 0.0313	0.9628 \pm 0.0082	0.9650 \pm 0.0366
LEAD	0.5827 \pm 0.1291	0.9224 \pm 0.0484	0.9568 \pm 0.0311
LCADNet	0.6427 \pm 0.1045	0.9500 \pm 0.0257	0.9657 \pm 0.0344
LERD	0.6891 \pm 0.1182	0.9500 \pm 0.0388	0.8383 \pm 0.0578

F. Architectures and Training Details

This section gives a concise description of the components used in LERD and the training protocol.

F.1. Input, preprocessing, and windowing

EEG is segmented into non-overlapping windows and z -scored channel-wise using statistics computed on the training split of each fold. In our AD experiments we use 2 s windows from 500 Hz recordings ($T=1000$) and $C=19$ electrodes (10–20 layout). Other datasets can adjust C and T without changing the architecture.

F.2. Encoder

The encoder follows the temporal-spatial factorization popular in EEGNet, with a mild max-norm constraint on spatial depthwise kernels for stability on EEG.

- **Block 1 (temporal \rightarrow spatial).** Depthwise temporal convolution \rightarrow BatchNorm \rightarrow ELU; then depthwise *spatial* convolution across electrodes \rightarrow BatchNorm \rightarrow ELU; time average pooling; dropout (0.1).
- **Block 2 (depthwise-separable temporal).** Depthwise temporal convolution \rightarrow BatchNorm \rightarrow ELU; pointwise mixing \rightarrow BatchNorm \rightarrow ELU; time average pooling; dropout (0.1).
- **Two branches.** (a) A flattened *main* feature vector is used by the classifier; (b) a temporally downsampled, per-electrode feature map feeds the EPDE/MELP/dLIF block.

F.3. EPDE + MELP + dLIF coupling (latent event dynamics)

Given the encoder’s per-electrode temporal features, the EPDE produces a differentiable posterior over next-event times. We parameterize a small MLP per channel to output mixture parameters for the **MELP** (lognormal mixture; $K=3$ components).

Module	Input	Output	Activation
Input window	$\mathbb{R}^{B \times 1 \times 19 \times 1000}$	–	–
Encoder (temporal branch)	$\mathbb{R}^{B \times 1 \times 19 \times 1000}$	$\mathbb{R}^{B \times 19 \times L}$ ($L = 250$)	ELU
Encoder (main branch, flattened)	$\mathbb{R}^{B \times 1 \times 19 \times 1000}$	$\mathbb{R}^{B \times 1178}$	ELU
EPDE/MELP/dLIF block	$\mathbb{R}^{B \times 19 \times L}$	$\mathbb{R}^{B \times 19 \times L}$	ELU (MLPs), Tanh (ODE)
ERG adjacency	lags from EPDE/MELP	$\mathbb{R}^{B \times 19 \times 19}$	exp kernel
GCN node embeddings	$\mathbb{R}^{B \times 19 \times L}$, adjacency	$\mathbb{R}^{B \times 19 \times 64}$	ReLU
Flattened graph features	$\mathbb{R}^{B \times 19 \times 64}$	$\mathbb{R}^{B \times 1216}$	–
Fusion vector	concat(main, graph)	$\mathbb{R}^{B \times 2394}$	–
Classifier logits	$\mathbb{R}^{B \times 2394}$	$\mathbb{R}^{B \times \mathcal{Y} }$	ReLU (hidden), Softmax (out)

Sampling is reparameterized during training; at test time we use mixture expectations. A compact hidden state is evolved with an explicit–Euler solver to obtain a denoised per–electrode trajectory used downstream. A rate proxy read from the EPDE is softly aligned with the **dLIF** prior via an L_2 rate consistency term with refractory gating and a plausible alpha/theta–to–beta frequency range.

F.4. Event–Relational Graph (ERG) and GCN

From posterior samples of event times, cross–channel lags are mapped through a smooth STDP–shaped nonlinearity to edge scores in $[0, 1]$, then averaged over time/samples to produce a symmetric adjacency. A weak Fisher– z alignment term biases edges toward observable correlations computed from the raw EEG without enforcing them. A single GCN layer converts per–channel temporal descriptors into compact node embeddings that are flattened for fusion.

F.5. Classifier and fusion

We concatenate the encoder’s main vector with the flattened GCN features and apply a two–layer MLP followed by a linear layer and Softmax over classes. No attention or recurrence is used at this stage; temporal information is already summarized by EPDE/MELP and the encoder.

F.6. Optimization and protocol

- **Loss.** Cross–entropy for labels plus small auxiliary terms: EPDE/MELP reconstruction/regularizers, dLIF rate consistency, ERG Fisher– z , and the IVP–KL surrogate. We use modest default weights and found them robust across cohorts.
- **Training.** Adam (lr 5×10^{-4} , weight decay 10^{-4}), batch size 1024, gradient–norm clipping at 1.0, 30 epochs. Learning rate is halved if validation AUC does not improve for 15 epochs; the best AUC checkpoint is kept.
- **Evaluation.** Five–fold *cross–subject* splits; subject–level predictions from window probabilities via majority vote (or simple averaging).

F.7. Shapes summary

Below we list only input/output sizes and activations for clarity; $L=250$ denotes the temporal length after the first time–pooling stage.

F.8. Pseudocode summaries

Algorithm 1 MELP Sampling (per electrode and time proxy)

Require: Mixture weights $w \in \Delta^{K-1}$, means $\mu \in \mathbb{R}^K$, standard deviations $\sigma \in \mathbb{R}_+^K$

Ensure: Inter–event interval $\tau \in \mathbb{R}_+$

- 1: Sample component $k \sim \text{Categorical}(w)$
 - 2: Sample noise $\epsilon \sim \mathcal{N}(0, 1)$
 - 3: $\tau \leftarrow \exp(\mu_k + \sigma_k \cdot \epsilon)$
 - 4: **return** τ
-

Algorithm 2 Neural ODE evolution over $[t_s, t_e]$ with S Euler sub-steps

Require: Features ξ , projection map $\text{proj}(\cdot)$, decoder $\text{decode}(\cdot)$, vector field $f(\cdot)$, residual weight $\alpha > 0$, sub-steps $S \in \mathbb{N}$, interval $[t_s, t_e]$

Ensure: Decoded trajectory $\hat{z} \in \mathbb{R}^{\lfloor T/4 \rfloor}$

- 1: $y_0 \leftarrow \text{proj}(\xi)$
 - 2: $\Delta t \leftarrow (t_e - t_s)/S$
 - 3: **for** $m = 0, 1, \dots, S - 1$ **do**
 - 4: $y_{m+1} \leftarrow y_m + \Delta t \cdot (f(y_m) + \alpha y_m)$
 - 5: **end for**
 - 6: $\hat{z} \leftarrow \text{decode}(y_S)$
 - 7: **return** \hat{z}
-

Algorithm 3 Graph weights from z_t

Require: Per-electrode trajectories $z_t \in \mathbb{R}^{N \times L}$ with $L = \lfloor T/4 \rfloor$; scale $\gamma > 0$; kernel mode $\text{mode} \in \{\text{exp, gauss, invl}\}$

Ensure: Symmetric adjacency $W \in \mathbb{R}^{N \times N}$ with zero diagonal

- 1: $\forall c \in \{1, \dots, N\} : s_c \leftarrow \frac{1}{L} \sum_{t=1}^L z_t(c, t)$
 - 2: **for** $i = 1, \dots, N$ **do**
 - 3: **for** $j = 1, \dots, N$ **do**
 - 4: **if** $i = j$ **then**
 - 5: $W_{ij} \leftarrow 0$
 - 6: **else**
 - 7: $\Delta \leftarrow |s_i - s_j|$
 - 8: $W_{ij} \leftarrow \exp(-\gamma \Delta)$
 - 9: **end if**
 - 10: **end for**
 - 11: **end for**
 - 12: $W \leftarrow \frac{1}{2} (W + W^\top)$ {Enforce symmetry}
 - 13: **return** W
-

Algorithm 4 LERD: Training and Inference

Require: Dataset $\mathcal{D} = \{(X, Y)\}$, electrodes C , window length T , MELP comps K , ODE substeps S

Require: Loss weights $\lambda_{\text{aux}}, \lambda_{\text{spk}}, \lambda_{\text{graph}}, \lambda_{\text{LIF}}$; LR η

Ensure: Trained params Θ ; predictor LERD(\cdot)

- 1: Initialize encoder ψ , EPDE+MELP ϕ , dLIF head ξ , ERG+GCN η_g , classifier θ ; Adam(η)
 - 2: **for** epoch = 1.. E **do**
 - 3: **for** mini-batch $(X, Y) \sim \mathcal{D}$ **do**
 - 4: **Preprocess:** channel-wise z -score per window
 - 5: **Encoder** (ψ): $\text{main_vec} \in \mathbb{R}^{B \times d_{\text{main}}}$, $\text{temp_feat} \in \mathbb{R}^{B \times C \times 1 \times L}$, $L = \lfloor T/4 \rfloor$
 - 6: **EPDE+MELP+ODE:**
 For $c = 1..C$: EPDE \Rightarrow mixture $(\mathbf{w}_c, \boldsymbol{\mu}_c, \boldsymbol{\sigma}_c)$; sample $\tau = \exp(\mu_{c,k} + \sigma_{c,k}\varepsilon)$, accumulate events $\{T_c\}$; ODE evolve with S Euler steps \Rightarrow trajectory $z_{c,\cdot}$
 - 7: Stack $Z \in \mathbb{R}^{B \times C \times L}$; keep event lags for ERG
 - 8: **dLIF prior:** compute $r_c(t)$ from Z with refractory gate; rate proxy $\hat{r}_c(t)$
 - 9: **Regularizers:** $\mathcal{R}_{\text{LIF}} = \sum_c \int (\hat{r}_c - r_c)^2$; $\text{KL}_T = \sum_c \mathcal{U}_\varepsilon(q_c \| p_{\text{dLIF}})$ (IVP-KL bound)
 - 10: **ERG** from event lags: $e_{ij}(t) = \exp(-\alpha |\Delta \tilde{t}_{ij}(t)|)$, average $\Rightarrow \bar{A}$
 - 11: **Fisher- z alignment:** $\mathcal{R}_{\text{ERG}} = \sum_{i < j} [(z_{ij}^{\text{obs}} - z_{ij}^{\text{pred}})^2 / (2\sigma_{ij}^2) + \frac{1}{2} \log \sigma_{ij}^2]$
 - 12: **GCN** on (\bar{A}, Z) : $G \in \mathbb{R}^{B \times (C \cdot d_g)}$; **Fuse** $H = [\text{main_vec}; G]$
 - 13: **Classifier:** logits $\ell = \text{MLP}(H)$, $p = \text{softmax}(\ell)$
 - 14: **Loss:** $\mathcal{L} = \text{CE}(p, Y) + \lambda_{\text{aux}} \mathcal{L}_{\text{STRODE}} + \lambda_{\text{spk}} \mathcal{L}_{\text{spk}} + \lambda_{\text{graph}} \mathcal{R}_{\text{ERG}} + \lambda_{\text{LIF}} \mathcal{R}_{\text{LIF}} + \text{KL}_T$
 - 15: Backprop; clip $\|\nabla\| \leq 1$; Adam step on Θ
 - 16: **end for**
 - 17: **end for**

 - 18: **Inference on window X :**
 - 19: Preprocess \rightarrow Encoder; EPDE gives MELP expectations \rightarrow events $\{T_c\}$; ODE $\rightarrow Z$; build \bar{A} ; GCN $\rightarrow G$; fuse $\rightarrow H$; output p and $\hat{y} = \arg \max p$
 - 20: **Subject aggregation:** majority vote $\Rightarrow \hat{y}_{\text{subj}}$
-